The Journal of Chemical Physics

Space partitioning of exchange-correlation functionals with the projector augmented-wave method

Cite as: J. Chem. Phys. **150**, 054101 (2019); https://doi.org/10.1063/1.5078432
Submitted: 25 October 2018 . Accepted: 11 January 2019 . Published Online: 01 February 2019

H. Levämäki, M. Kuisma, and K. Kokko

The Journal of Chemical Physics ARTICLE scitation.org/journal/jcp

Space partitioning of exchange-correlation functionals with the projector augmented-wave method

Cite as: J. Chem. Phys. 150, 054101 (2019); doi: 10.1063/1.5078432
Submitted: 25 October 2018 • Accepted: 11 January 2019 •
Published Online: 1 February 2019

H. Levämäki,[1,a)] M. Kuisma,[2] and K. Kokko[3,4]

AFFILIATIONS

[1]Applied Materials Physics, Department of Materials Science and Engineering, Royal Institute of Technology, Stockholm SE-100 44, Sweden
[2]Department of Chemistry, Nanoscience Center, University of Jyväskylä, P.O. Box 35, FIN-40014 Jyväskylä, Finland
[3]Department of Physics and Astronomy, University of Turku, FI-20014 Turku, Finland
[4]Turku University Centre for Materials and Surfaces (MatSurf), FI-20014 Turku, Finland

[a)]**Electronic mail:** levamaki@kth.se

ABSTRACT

We implement a Becke fuzzy cells type space partitioning scheme for the purposes of exchange-correlation within the GPAW projector augmented-wave method based density functional theory code. Space partitioning is needed in the situation where one needs to treat different parts of a combined system with different exchange-correlation functionals. For example, bulk and surface regions of a system could be treated with functionals that are specifically designed to capture the distinct physics of those regions. Here, we use the space partitioning scheme to implement the quasi-nonuniform exchange-correlation scheme, which is a useful practical approach for calculating metallic alloys on the generalized gradient approximation level. We also confirm the correctness of our implementation with a set of test calculations.

I. INTRODUCTION

Density functional theory (DFT)[1,2] has become a standard technique for the computation of electronic properties of molecules and periodic systems. As a theory, DFT is exact, but in practical calculations, one of the functionals, the exchange-correlation (XC) functional, has to be always approximated. One of the great strengths of DFT is that even the simplest XC approximation, the local density approximation (LDA),[2–5] turned out to be remarkably useful, albeit mostly for physics related applications and to a lesser degree for chemistry. The next family of XC approximations beyond the LDA are generalized gradient approximations (GGAs), which offer fairly ubiquitous improvements over LDA. One of the most well-known GGA XC functionals is the Perdew-Burke-Ernzerhof (PBE) functional,[6] which has earned itself the rank of a "standard functional." Although even more sophisticated XC approximations, such as meta-GGAs[7–9] and hybrid XC functionals,[10,11] are being developed and further improved, GGAs are still the most sensible choice for many applications due to their excellent computational speed versus accuracy ratio.

The potential accuracy of GGAs, however, has a certain ceiling because the information that a GGA functional has about any given system is limited to the electron density n and the gradient of the density ∇n. This deals with the computation of periodic and solid-state systems on the GGA level, and in this realm, there exists evidence that we might be approaching the accuracy limit. For example, a recent paper by Tran *et al.*[12] benchmarks various GGAs on their accuracy for a set of important solid-state properties. Equilibrium lattice constant is one of the most fundamental properties in solid-state physics, and Fig. 4 of the work of Tran *et al.* shows that modern solid-state GGAs (WC,[13] PBEsol,[14] SOGGA,[15] and SG4[16]) are all clustering above a mean absolute relative error (MARE) of about 0.5%. This suggests that the MARE of

~0.5% represents an accuracy barrier that has proved difficult to breach on the GGA level. The accuracy limit of GGA functionals has important consequences. In the work of Tian *et al.*,[17] it has been discussed why GGA functionals often yield poor formation energies for metallic binary alloys, and the reason is connected to the GGA lattice constant accuracy limit. An accurate formation energy requires that the equation of states (and therefore lattice constants) of all alloy components are described accurately. On the GGA level, this is often impossible.

In this paper, we utilize the "fuzzy cells" space partitioning concept of Becke[18] to circumvent the accuracy limit of the GGA level by implementing a space partitioned GGA XC functional quasi-nonuniform approximation (QNA)[19,20] within the state-of-the-art electronic structure code GPAW.[21,22] Our starting point is the PBE-family (PBE, PBEsol), whose functionality is governed by two parameters noted as μ and β. The parameter μ gives the strength of GGA corrections over LDA exchange and β gives the strength of corrections over LDA correlation. Thus, in general, an accurate description of XC effects only with a semi-local description of PBE-ansatz with energy functional $E_{xc}[n(\mathbf{r});\mu,\beta] = \int d\mathbf{r} n(\mathbf{r})\epsilon(n(\mathbf{r}), |\nabla n(\mathbf{r})|^2, \mu, \beta)$ is not possible, where ϵ is the XC energy per particle. A generic element within chemistry is obviously a single atom, and without any external fields, the external potential $v_{ext}(\mathbf{r})$ is solely a function of the atomic positions. Especially in the case of solid alloys with metallic bonds, we consider improving GGA by explicitly parametrising it in a volume around each atom species. In this approach, called quasi-nonuniform approximation (QNA),[19,20] the XC functional is no longer a density functional theory in a strict sense, but becomes also a function of atomic positions and information of species $E_{xc}^{QNA}[n; \{(\mathbf{R}^a, \mu^a, \beta^a)\}] = \int d\mathbf{r} n(\mathbf{r})\epsilon_{QNA}(n(\mathbf{r}), |\nabla n(\mathbf{r})|^2, \{(\mathbf{R}^a, \mu^a, \beta^a)\})$, where $\mathbf{R}^a$ is the atomic position, and μ^a and β^a are atom-specific parameters described later in the text. The approach has been previously implemented in the exact muffin-tin orbitals (EMTO) method,[23–26] and good results have been obtained for various binary alloys.[17] However, in the original implementation, volumes with a strict Voronoi partition were used, rendering the local PBE-ansatz parameters discontinuous with respect to $\mathbf{r}$. Here, we overcome the difficulty by employing the fuzzy cells space partitioning concept of Becke,[18] which allows the computation of analytic QNA forces and stress tensor. For efficient calculations, we implement the projector augmented wave method corrections[27,28] to QNA within the projector augmented-wave method based DFT code GPAW. Atomic Simulation Environment (ASE)[29,30] is used throughout the article for handling the atomic geometries and optimizations.

II. IMPLEMENTATION

The QNA scheme essentially generalizes the μ and β parameters of PBE XC functional[6] into space dependent $\mu(\mathbf{r})$ and $\beta(\mathbf{r})$ fields

$$\mu(\mathbf{r}) = \sum_a w_a(\mathbf{r})\mu^a, \tag{1}$$

$$\beta(\mathbf{r}) = \sum_a w_a(\mathbf{r})\beta^a, \tag{2}$$

where μ^a and β^a are optimized parameters corresponding to a given element occupying atomic site a. Consequently, the QNA XC energy can be written in the form

$$E_{XC}^{QNA}[n] = \int n(\mathbf{r})\varepsilon_{XC}^{PBE}[n(\mathbf{r}), |\nabla n(\mathbf{r})|^2, \mu(\mathbf{r}), \beta(\mathbf{r})]\, d\mathbf{r}, \tag{3}$$

where

$$\epsilon_{XC}^{PBE} = \varepsilon_X^{LDA}\left(F_X^{PBE}[n(\mathbf{r}), |\nabla n(\mathbf{r})|^2, \mu(\mathbf{r})] + \left\{\frac{\varepsilon_C^{LDA}}{\varepsilon_X^{LDA}} + \frac{H[n(\mathbf{r}), |\nabla n(\mathbf{r})|^2, \beta(\mathbf{r})]}{\varepsilon_X^{LDA}}\right\}\right) \tag{4}$$

is the PBE-type XC energy density per particle. The $\mu(\mathbf{r})$ and $\beta(\mathbf{r})$ fields should interpolate sharply between atoms and, in practice, this creates the need to divide space into Voronoi-type atomic site centered regions. Space division can be accomplished by appropriate weight fields $w_a(\mathbf{r})$. The value of $w_a(\mathbf{r})$ should approach unity close to atomic site a and decay smoothly to zero away from site a. Additionally, it must always hold that $\sum_a w_a(\mathbf{r}) = 1$. We define the weights as

$$w_a(\mathbf{r}) = \frac{P_a(\mathbf{r})}{\sum_{a'} P_{a'}(\mathbf{r})}, \tag{5}$$

which follows the fuzzy cells concept first developed by Becke.[18] In the fuzzy cells scheme, $P_a(\mathbf{r})$ are atomic site centered partial weights, which have the value one at the atomic site $\mathbf{R}^a$ and decay to zero when the distance $|\mathbf{r} - \mathbf{R}^a|$ becomes large. $P_a(\mathbf{r})$ could be defined in many different ways, but here we will use

$$P_a(\mathbf{r}) = f(|\mathbf{r} - \mathbf{R}^a|) = \exp\left[-\left(\frac{|\mathbf{r} - \mathbf{R}^a|}{\lambda}\right)^{2\alpha}\right], \tag{6}$$

which is very similar to the expression developed in Ref. 31. The parameter λ controls the location of the transition from 1 to 0, and α controls the sharpness of the transition. We have found that values $\lambda = 1.2$ and $\alpha = 2.0$ give partitioning that is very close to the exact Voronoi cells and also the most accurate formation energies. The calibration of formation energies has been done by calculating the formation energies of ordered Cu_3Au and $CuAu_3$ ($L1_2$), and CuAu ($L1_0$) and then comparing them to previous EMTO QNA results.[32]

For periodic and solid-state calculations, the expression of Eq. (6), and that of Ref. 31, for $P_a(\mathbf{r})$ is particularly beneficial because the computational load of Eq. (6) scales only linearly as a function of nuclei. This is in contrast to the quadratic scaling of the original Becke form and others,[33] which are often used in chemistry. Chemistry calculations routinely employ a computationally heavy hybrid XC functional, which means a quadratic scaling $P_a(\mathbf{r})$ is responsible for only a fraction of the total computational load. However, in solid state physics, fast semilocal LDA and GGA XC functionals are popular, which can easily cause a quadratic scaling $P_a(\mathbf{r})$ to become a computational bottleneck.

Performing geometric relaxations using the QNA scheme requires the computation of forces and the stress tensor. For an all-electron case, the XC potential can be evaluated in the usual fashion as

$$v_{\mathrm{xc}}(\mathbf{r}) = \frac{\delta \mathrm{E}_{\mathrm{XC}}^{\mathrm{PBE}}[n(\mathbf{r}), \mu(\mathbf{r}), \beta(\mathbf{r})]}{\delta n(\mathbf{r})}, \tag{7}$$

where the dependence on $\mu(\mathbf{r})$ and $\beta(\mathbf{r})$ is purely parametric as they are not explicit functions of density but of nuclear coordinates. This equation is now in useful form, as it allows simple analytical gradients.

We now consider the projector augmented wave method implementation and begin with a brief introduction of relevant concepts. The general idea in projector aumented-wave (PAW) methods is that the Kohn–Sham equations are solved for smooth wave functions ($\tilde{\psi}_n(\mathbf{r})$), but retaining one-to-one mapping with the all-electron wave functions ($\psi_n(\mathbf{r})$). There exists a linear PAW transformation operator which defines a mapping $\psi_n(\mathbf{r}) = \mathcal{T}\tilde{\psi}_n(\mathbf{r})$, and the Kohn–Sham equations are derived to be $\mathcal{T}^\dagger \mathrm{H} \mathcal{T} \tilde{\psi}_n(\mathbf{r}) = \mathcal{T}^\dagger \mathcal{T} \tilde{\psi}_n(\mathbf{r})$.

A key quantity is the pseudo electron density (we consider spin paired systems here for simplicity)

$$\tilde{n}(\mathbf{r}) = \tilde{n}_{\mathrm{c}}(\mathbf{r}) + \sum_i f_i |\tilde{\psi}_n(\mathbf{r})|^2, \tag{8}$$

and the corresponding all-electron density is

$$n(\mathbf{r}) = n_{\mathrm{c}}(\mathbf{r}) + \sum_n f_n |\mathcal{T}\tilde{\psi}_n(\mathbf{r})|^2 = n_{\mathrm{c}}(\mathbf{r}) + \sum_n f_n |\psi_n(\mathbf{r})|^2, \tag{9}$$

where f_n are the occupation numbers, $\tilde{n}_{\mathrm{c}}$ is the pseudo core density, and n_{c} is the all-electron core density for the frozen core approximation.

In the PAW-formalism, a local quantity has three useful definitions varying in domain and whether they are pseudo quantities or not. For example, to utilize density thoroughly in all circumstances required by implementation, three quantities are needed. In the case of density, they are the pseudo density $\tilde{n}(\mathbf{r})$, atom-centered pseudo densities for each atom $\{\tilde{n}^a(\mathbf{r})\}$, and atom-centered all electron densities $\{n^a(\mathbf{r})\}$. The domains in the GPAW code are such that in the grid, LCAO, and plane wave modes, the pseudo density $\tilde{n}(\mathbf{r})$ is defined in Cartesian real space grid with grid-spacing typically between 0.07 and 0.15 Å. Furthermore, the pseudo ($\tilde{n}^a(\mathbf{r})$) and all-electron densities ($n^a(\mathbf{r})$) are defined within logarithmic radial grid and their angular parts are expanded using 50 Lebedev points. For $r > r_{\mathrm{c}}$, where r_{c} is the PAW cutoff of an atomic augmentation sphere, it holds that $\tilde{n}^a(\mathbf{r}) = n^a(\mathbf{r})$ with their derivatives at $|r| = r_{\mathrm{c}}$ being also matched. Inside the augmentation spheres, $n^a(\mathbf{r})$ and $\tilde{n}^a(\mathbf{r})$ will of course differ. The three density definitions are connected to each other by the equation

$$n(\mathbf{r}) = \tilde{n}(\mathbf{r}) + \sum_a (n^a(\mathbf{r}) - \tilde{n}^a(\mathbf{r})), \tag{10}$$

which means that the all-electron density is obtained from the pseudo density by subtracting the atom-centered pseudo densities and then adding the atom-centered all-electron densities. From Eq. (10), it is easy to see that outside the augmentation spheres ($r > r_{\mathrm{c}}$) $n(\mathbf{r}) = \tilde{n}(\mathbf{r})$. The crux of PAW implementation of QNA is to define analogous quantities to the previous density example, which are $\tilde{\mu}(\mathbf{r})$, $\tilde{\mu}^a(\mathbf{r})$ and $\mu^a(\mathbf{r})$, and $\tilde{\beta}(\mathbf{r})$, $\tilde{\beta}^a(\mathbf{r})$ and $\beta^a(\mathbf{r})$, respectively. These μ and β quantities also fulfill Eq. (10). At later stage, we will perform an approximation $\tilde{\mu}^a(\mathbf{r}) = \mu^a(\mathbf{r}) = \mu^a$, where μ^a is the constant optimal μ parameter of an element at atomic site a, and discuss the accuracy of this approximation. However, for completeness, we now proceed with the derivation without such approximations, i.e., $\tilde{\mu}(\mathbf{r})$, $\tilde{\mu}^a(\mathbf{r})$, and $\mu^a(\mathbf{r})$ are all equal to $\mu(\mathbf{r})$ of Eq. (1) within the domains they are defined in and similarly for β quantities.

The energy gradients in the PAW formalism can be in general written as

$$\begin{aligned}\mathbf{F}^a &= -\frac{\mathrm{dE}}{\mathrm{d}\mathbf{R}^a} = -\frac{\partial \mathrm{E}}{\partial \mathbf{R}^a} - \sum_n \left(\int \mathrm{d}\mathbf{r} \frac{\partial \mathrm{E}}{\partial \tilde{\psi}_n(\mathbf{r})} \frac{\mathrm{d}\tilde{\psi}_n(\mathbf{r})}{\mathrm{d}\mathbf{R}^a} + \mathrm{h.c.} \right) \\ &= -\frac{\partial \mathrm{E}}{\partial \mathbf{R}^a} + \sum_n f_n \epsilon_n \langle \tilde{\psi}_n | \frac{\mathrm{d}\hat{\mathrm{S}}}{\mathrm{d}\mathbf{R}^a} | \tilde{\psi}_n \rangle, \end{aligned} \tag{11}$$

where "h.c." denotes the Hermitian conjugate and $\hat{\mathrm{S}}$ is the overlap operator $\mathcal{T}^\dagger \mathcal{T}$ [Eq. (48) of Ref. 21]. The QNA XC functional does not have explicit wave function dependence and hence we only need to consider the partial derivative $-\frac{\mathrm{dE}}{\mathrm{d}\mathbf{R}^a}$. For local and semi-local functionals, the XC energy in the PAW formalism can be written as

$$\begin{aligned}\mathrm{E}_{\mathrm{XC}} = \mathrm{E}_{\mathrm{XC}}[\tilde{n}(\mathbf{r}), \tilde{\mu}(\mathbf{r}), \tilde{\beta}(\mathbf{r})] + \sum_a \mathrm{E}^a_{\mathrm{XC}}[n^a(\mathbf{r}), \mu^a(\mathbf{r}), \beta^a(\mathbf{r})] \\ - \mathrm{E}^a_{\mathrm{XC}}[\tilde{n}^a(\mathbf{r}), \tilde{\mu}^a(\mathbf{r}), \tilde{\beta}^a(\mathbf{r})], \end{aligned} \tag{12}$$

where the term

$$\Delta \mathrm{E}^a = \mathrm{E}_{\mathrm{XC}}[n^a[\mathrm{D}^a_{ii'}], \mu^a(\mathbf{r}), \beta^a(\mathbf{r})] - \mathrm{E}_{\mathrm{XC}}[\tilde{n}^a[\mathrm{D}^a_{ii'}], \tilde{\mu}^a(\mathbf{r}), \tilde{\beta}^a(\mathbf{r})] \tag{13}$$

is typically called the PAW-correction and it introduces the atomic density matrix as defined in Ref. 34. By taking the partial derivative with respect to the nuclear position of Eq. (12), we arrive at Eq. (A1), which is presented in Appendix A. The first term in the right-hand side of Eq. (A1) is already handled by GPAW, and it is solved by noting that in Eq. (8), only the pseudo core density $\tilde{n}_{\mathrm{c}}(\mathbf{r})$ depends on atomic positions, i.e.,

$$-\int \mathrm{d}\mathbf{r} \frac{\delta \mathrm{E}_{\mathrm{XC}}[\tilde{n}]}{\delta \tilde{n}(\mathbf{r})} \frac{\partial \tilde{n}(\mathbf{r})}{\partial \mathbf{R}^a} = -\int \mathrm{d}\mathbf{r} \frac{\delta \mathrm{E}_{\mathrm{XC}}[\tilde{n}]}{\delta \tilde{n}(\mathbf{r})} \frac{\partial \tilde{n}_{\mathrm{c}}(\mathbf{r})}{\partial \mathbf{R}^a}. \tag{14}$$

Furthermore, the density functional derivatives of the form $\delta E/\delta n$ in Eq. (14) or via the atomic wise quantities in Eq. (A1) are readily evaluated in GPAW via the typical Euler-Lagrange derivation

$$v_{XC}(\mathbf{r}) = \frac{\delta E_{XC}[n(\mathbf{r})]}{\delta n(\mathbf{r})} = \frac{\partial(n(\mathbf{r})\epsilon_{XC}[n(\mathbf{r}),\nabla n(\mathbf{r})])}{\partial n(\mathbf{r})} - \nabla\cdot\left(\frac{\partial(n(\mathbf{r})\epsilon_{XC}[n(\mathbf{r}),\nabla n(\mathbf{r})])}{\partial\nabla n(\mathbf{r})}\right) = \frac{\partial(n(\mathbf{r})\epsilon_{XC}[n(\mathbf{r}),\nabla n(\mathbf{r})])}{\partial n(\mathbf{r})} - \nabla\cdot\left(\frac{\partial(n(\mathbf{r})\epsilon_{XC}[n(\mathbf{r}),\sigma(\mathbf{r})])}{\partial\sigma(\mathbf{r})}2\nabla n(\mathbf{r})\right), \quad (15)$$

where $\sigma(\mathbf{r}) = |\nabla n(\mathbf{r})|^2$.

Thus, regarding the new implementation of QNA forces, we are left with only the partial derivatives with respect to various μ and β parameters. Due to the atomic site centered $\mu(\mathbf{r})$ and $\beta(\mathbf{r})$ fields, E_{XC}^{QNA} has an additional dependency on the positions of the nuclei, which created the extra derivative chain rules in Eq. (A1). We have now derived the QNA-XC force exactly, given that all quantities $\tilde{\mu}(\mathbf{r})$, $\tilde{\mu}^a(\mathbf{r})$, and $\mu^a(\mathbf{r})$ are equal to all-electron definition [Eq. (1)] within their domains of definition. However, it is cumbersome to calculate $\tilde{\mu}^a(\mathbf{r})$ within the logarithmic radial grid using the definition of Eq. (1). To this end, we make a typical approximation, where a quantity almost constant within an augmentation sphere is assumed to be constant. In other words, we set $\tilde{\mu}^a(\mathbf{r}) = \mu^a(\mathbf{r}) = \mu^a$. Outside the augmentation sphere, the fact that $\tilde{\mu}^a(\mathbf{r})$ deviates from μ^a does not matter, since the correction vanishes because $n^a(\mathbf{r}) = \tilde{n}^a(\mathbf{r})$ there also. Inside the augmentation sphere, where $n^a(\mathbf{r})$ and $\tilde{n}^a(\mathbf{r})$ deviate, the region is so close to atom a that the μ^a term dominates in Eq. (1). Consequently, we circumvent the need to use Eq. (1) as defined within the logarithmic radial grids, which simplifies practical calculations. The argumentation of this paragraph is trivially extended to $\tilde{\beta}(\mathbf{r})$, $\tilde{\beta}^a(\mathbf{r})$, and $\beta^a(\mathbf{r})$ as well.

With these approximations, the QNA XC becomes

$$E_{XC} = E_{XC}[\tilde{n}(\mathbf{r}),\tilde{\mu}(\mathbf{r}),\tilde{\beta}(\mathbf{r})] + \sum_a E_{XC}^a[n^a(\mathbf{r}),\mu^a,\beta^a] - E_{XC}^a[\tilde{n}^a(\mathbf{r}),\tilde{\mu}^a,\tilde{\beta}^a] \quad (16)$$

and the forces simplify to

$$\mathbf{F}_{XC}^a = -\int d\mathbf{r}\left(\frac{\delta E_{XC}[\tilde{n}(\mathbf{r}),\tilde{\mu}(\mathbf{r}),\tilde{\beta}(\mathbf{r})]}{\delta\tilde{n}(\mathbf{r})}\frac{\partial\tilde{n}(\mathbf{r})}{\partial\mathbf{R}^a} + \frac{\delta E_{XC}[\tilde{n}(\mathbf{r}),\tilde{\mu}(\mathbf{r}),\tilde{\beta}(\mathbf{r})]}{\delta\tilde{\mu}(\mathbf{r})}\frac{\partial\tilde{\mu}(\mathbf{r})}{\partial\mathbf{R}^a} + \frac{\delta E_{XC}[\tilde{n}(\mathbf{r}),\tilde{\mu}(\mathbf{r}),\tilde{\beta}(\mathbf{r})]}{\delta\tilde{\beta}(\mathbf{r})}\frac{\partial\tilde{\beta}(\mathbf{r})}{\partial\mathbf{R}^a}\right) - \sum_a\sum_{ii'}\int d\mathbf{r}\left(\frac{\delta E_{XC}^a[n^a(\mathbf{r}),\mu^a,\beta^a]}{\delta n^a(\mathbf{r})}\frac{\partial n^a(\mathbf{r})}{\partial D_{ii'}^a} + \frac{\delta E_{XC}^a[\tilde{n}^a(\mathbf{r}),\mu^a,\beta^a]}{\delta\tilde{n}^a(\mathbf{r})}\frac{\partial n^a(\mathbf{r})}{\partial D_{ii'}^a}\right)\frac{\partial D_{ii'}^a}{\partial\mathbf{R}^a}. \quad (17)$$

At this point, we can readily evaluate the remaining partial derivatives

$$\frac{\delta E_{XC}^{PBE}}{\delta\tilde{\mu}(\mathbf{r})}\frac{\partial\tilde{\mu}(\mathbf{r})}{\partial\mathbf{R}^a} = \int\frac{\partial\left\{\tilde{n}(\mathbf{r})\varepsilon_{XC}^{PBE}[\tilde{n}(\mathbf{r}),|\nabla\tilde{n}(\mathbf{r})|^2,\tilde{\mu}(\mathbf{r}),\tilde{\beta}(\mathbf{r})]\right\}}{\partial\tilde{\mu}(\mathbf{r})} \times\sum_{a'}\frac{\partial w_{a'}(\mathbf{r})}{\partial\mathbf{R}^a}\mu^{a'}\,d\mathbf{r}, \quad (18)$$

$$\frac{\delta E_{XC}^{PBE}}{\delta\tilde{\beta}(\mathbf{r})}\frac{\partial\tilde{\beta}(\mathbf{r})}{\partial\mathbf{R}^a} = \int\frac{\partial\left\{\tilde{n}(\mathbf{r})\varepsilon_{XC}^{PBE}[\tilde{n}(\mathbf{r}),|\nabla\tilde{n}(\mathbf{r})|^2,\tilde{\mu}(\mathbf{r}),\tilde{\beta}(\mathbf{r})]\right\}}{\partial\tilde{\beta}(\mathbf{r})} \times\sum_{a'}\frac{\partial w_{a'}(\mathbf{r})}{\partial\mathbf{R}^a}\beta^{a'}\,d\mathbf{r}. \quad (19)$$

In Eqs. (18) and (19), we have the further partial derivatives

$$\frac{\partial\left\{n\varepsilon_{XC}^{PBE}\right\}}{\partial\tilde{\mu}(\mathbf{r})}, \quad \frac{\partial\left\{n\varepsilon_{XC}^{PBE}\right\}}{\partial\tilde{\beta}(\mathbf{r})}$$

and they have been written out in Appendix A. In order to get the $\delta w_{a'}(\mathbf{r})/\delta\mathbf{R}^a$ derivatives in Eqs. (18) and (19), we notice that

$$P_{a'}(\mathbf{r}) = f\left(\sqrt{(r_x - R_x^{a'})^2 + (r_y - R_y^{a'})^2 + (r_z - R_z^{a'})^2}\right), \quad (20)$$

which gives, for example,

$$\frac{\partial P_{a'}(\mathbf{r})}{\partial R_x^a} = -\delta_{aa'}f'(\sqrt{\cdots})\frac{(r_x - R_x^a)}{|\mathbf{r} - \mathbf{R}^a|} = -\delta_{aa'}\frac{\partial P_a(\mathbf{r})}{\partial r_x}. \quad (21)$$

The whole gradient with respect to $\mathbf{R}^a$ ($\nabla_{\mathbf{R}^a}$) is therefore easily obtained from the gradient of $\mathbf{r}$ using the ∇ operator

$$\frac{\partial P_{a'}(\mathbf{r})}{\partial\mathbf{R}^a} = \delta_{aa'}\nabla_{\mathbf{R}^a}P_a(\mathbf{r}) = -\delta_{aa'}\frac{\partial P_a(\mathbf{r})}{\partial\mathbf{r}} = -\delta_{aa'}\nabla P_a(\mathbf{r}). \quad (22)$$

Using Eq. (22), we obtain the following expression for the $\delta w_{a'}(\mathbf{r})/\delta\mathbf{R}^a$ derivatives:

$$\frac{\partial w_{a'}(\mathbf{r})}{\partial\mathbf{R}^a} = \frac{\partial}{\partial\mathbf{R}^a}\frac{P_{a'}(\mathbf{r})}{\sum_{a''}P_{a''}(\mathbf{r})} = \frac{\frac{\partial P_{a'}(\mathbf{r})}{\partial\mathbf{R}^a}\sum_{a''}P_{a''}(\mathbf{r}) - P_{a'}(\mathbf{r})\sum_{a''}\frac{\partial P_{a''}(\mathbf{r})}{\partial\mathbf{R}^a}}{\left[\sum_{a''}P_{a''}(\mathbf{r})\right]^2} = \frac{-\delta_{aa'}\nabla P_a(\mathbf{r})\sum_{a''}P_{a''}(\mathbf{r}) + P_{a'}(\mathbf{r})\nabla P_a(\mathbf{r})}{\left[\sum_{a''}P_{a''}(\mathbf{r})\right]^2}. \quad (23)$$

The stress tensor is needed in order to relax the unit cell. Analogous to the case of forces, additional terms will manifest in the stress tensor formula because the $\mu(\mathbf{r})$ and $\beta(\mathbf{r})$ fields

change as a function of strain. The derivations up to the end of this section make use of Ref. 35 which explores the computation of various stress tensor contributions in detail. Stress tensor σ is defined as a first order change under a strain ϵ as

$$\sigma_{\alpha\beta} = \frac{1}{\mathrm{V}} \frac{\partial \mathrm{E_{tot}}}{\partial \epsilon_{\alpha\beta}}. \tag{24}$$

Since the XC energy is an integral in real space, it can be shown that the XC contribution to the total stress tensor can be written as

$$\mathrm{V}\sigma^{\mathrm{XC}}_{\alpha\beta} = \frac{\partial \mathrm{E_{XC}}}{\partial \epsilon_{\alpha\beta}} = \delta_{\alpha\beta}\mathrm{E_{XC}} + \int_{\mathrm{V}} \frac{\partial[n(\mathbf{r})\varepsilon_{\mathrm{XC}}(\mathbf{r})]}{\partial \epsilon_{\alpha\beta}}\,\mathrm{d}\mathbf{r}. \tag{25}$$

For simplicity, here we drop the pseudo (~) notation and just use generic $\mu(\mathbf{r})$ and $\beta(\mathbf{r})$. Then the application of the chain rule to Eq. (25) gives

$$\begin{aligned}
&\int_{\mathrm{V}} \frac{\partial\{n(\mathbf{r})\varepsilon^{\mathrm{PBE}}_{\mathrm{XC}}[n(\mathbf{r}), |\nabla n(\mathbf{r})|^2, \mu(\mathbf{r}), \beta(\mathbf{r})]\}}{\partial \epsilon_{\alpha\beta}}\,\mathrm{d}\mathbf{r} \\
&\quad = \int_{\mathrm{V}} \frac{\partial\{n(\mathbf{r})\varepsilon^{\mathrm{PBE}}_{\mathrm{XC}}[n(\mathbf{r}), |\nabla n(\mathbf{r})|^2, \mu(\mathbf{r}), \beta(\mathbf{r})]\}}{\partial n(\mathbf{r})} \frac{\partial n(\mathbf{r})}{\partial \epsilon_{\alpha\beta}}\,\mathrm{d}\mathbf{r} && (26) \\
&\quad + \int_{\mathrm{V}} \frac{\partial\{n(\mathbf{r})\varepsilon^{\mathrm{PBE}}_{\mathrm{XC}}[n(\mathbf{r}), |\nabla n(\mathbf{r})|^2, \mu(\mathbf{r}), \beta(\mathbf{r})]\}}{\partial \nabla n(\mathbf{r})} \cdot \frac{\partial \nabla n(\mathbf{r})}{\partial \epsilon_{\alpha\beta}}\,\mathrm{d}\mathbf{r} && (27) \\
&\quad + \int_{\mathrm{V}} \frac{\partial\{n(\mathbf{r})\varepsilon^{\mathrm{PBE}}_{\mathrm{XC}}[n(\mathbf{r}), |\nabla n(\mathbf{r})|^2, \mu(\mathbf{r}), \beta(\mathbf{r})]\}}{\partial \mu(\mathbf{r})} \frac{\partial \mu(\mathbf{r})}{\partial \epsilon_{\alpha\beta}}\,\mathrm{d}\mathbf{r} && (28) \\
&\quad + \int_{\mathrm{V}} \frac{\partial\{n(\mathbf{r})\varepsilon^{\mathrm{PBE}}_{\mathrm{XC}}[n(\mathbf{r}), |\nabla n(\mathbf{r})|^2, \mu(\mathbf{r}), \beta(\mathbf{r})]\}}{\partial \beta(\mathbf{r})} \frac{\partial \beta(\mathbf{r})}{\partial \epsilon_{\alpha\beta}}\,\mathrm{d}\mathbf{r}. && (29)
\end{aligned}$$

In Eqs. (30)–(33) we expand each term one at a time (function arguments are dropped for simplicity). Equation (26) is the LDA-level term and it can be written as

$$\int_{\mathrm{V}} \frac{\partial\{n\varepsilon^{\mathrm{PBE}}_{\mathrm{XC}}\}}{\partial n} \frac{\partial n}{\partial \epsilon_{\alpha\beta}}\,\mathrm{d}\mathbf{r} = \int_{\mathrm{V}} \frac{\partial n}{\partial \epsilon_{\alpha\beta}} \left[\varepsilon^{\mathrm{PBE}}_{\mathrm{XC}} + n\frac{\partial \varepsilon^{\mathrm{PBE}}_{\mathrm{XC}}}{\partial n}\right]\mathrm{d}\mathbf{r}. \tag{30}$$

Equation (27) is the GGA-level gradient term and it can be written as

$$\begin{aligned}
\int_{\mathrm{V}} \frac{\partial\{n\varepsilon^{\mathrm{PBE}}_{\mathrm{XC}}\}}{\partial \nabla n} \cdot \frac{\partial \nabla n}{\partial \epsilon_{\alpha\beta}}\,\mathrm{d}\mathbf{r} &= \int_{\mathrm{V}} n\frac{\partial \varepsilon^{\mathrm{PBE}}_{\mathrm{XC}}}{\partial \nabla n} \cdot \frac{\partial \nabla n}{\partial \epsilon_{\alpha\beta}}\,\mathrm{d}\mathbf{r} \\
&= \int_{\mathrm{V}} n\frac{\partial \varepsilon^{\mathrm{PBE}}_{\mathrm{XC}}}{\partial |\nabla n|^2}\left(\frac{\partial |\nabla n|^2}{\partial \nabla n}\right) \cdot \left(\frac{\partial \nabla n}{\partial \epsilon_{\alpha\beta}}\right)\mathrm{d}\mathbf{r} \\
&= 2\int_{\mathrm{V}} n\frac{\partial \varepsilon^{\mathrm{PBE}}_{\mathrm{XC}}}{\partial |\nabla n|^2}(\nabla n) \cdot \left(\frac{\partial \nabla n}{\partial \epsilon_{\alpha\beta}}\right)\mathrm{d}\mathbf{r}, \qquad (31)
\end{aligned}$$

where we have used the fact that $\partial|\nabla n|^2/\partial\nabla n = 2\nabla n$. These LDA and GGA terms are already handled by GPAW. Equation (28) arises from the fact that the $\mu(\mathbf{r})$ field changes as a function of strain and it can be written as

$$\begin{aligned}
\int_{\mathrm{V}} \frac{\partial\{n\varepsilon^{\mathrm{PBE}}_{\mathrm{XC}}\}}{\partial \mu} \frac{\partial \mu}{\partial \epsilon_{\alpha\beta}}\,\mathrm{d}\mathbf{r} &= \int_{\mathrm{V}} n\frac{\partial \varepsilon^{\mathrm{PBE}}_{\mathrm{XC}}}{\partial \mu} \sum_a \frac{\partial w_a}{\partial \epsilon_{\alpha\beta}}\mu^a\,\mathrm{d}\mathbf{r} \\
&= \int_{\mathrm{V}} n\varepsilon^{\mathrm{LDA}}_{\mathrm{X}}\frac{\partial \mathrm{F}^{\mathrm{PBE}}_{\mathrm{X}}}{\partial \mu} \sum_a \frac{\partial w_a}{\partial \epsilon_{\alpha\beta}}\mu^a\,\mathrm{d}\mathbf{r}. \qquad (32)
\end{aligned}$$

Equation (29) is the $\beta(\mathbf{r})$ field change and it can be written as

$$\begin{aligned}
\int_{\mathrm{V}} \frac{\partial\{n\varepsilon^{\mathrm{PBE}}_{\mathrm{XC}}\}}{\partial \beta} \frac{\partial \beta}{\partial \epsilon_{\alpha\beta}}\,\mathrm{d}\mathbf{r} &= \int_{\mathrm{V}} n\frac{\partial \varepsilon^{\mathrm{PBE}}_{\mathrm{XC}}}{\partial \beta} \sum_a \frac{\partial w_a}{\partial \epsilon_{\alpha\beta}}\beta^a\,\mathrm{d}\mathbf{r} \\
&= \int_{\mathrm{V}} n\frac{\partial \mathrm{H}}{\partial \beta} \sum_a \frac{\partial w_a}{\partial \epsilon_{\alpha\beta}}\beta^a\,\mathrm{d}\mathbf{r}. \qquad (33)
\end{aligned}$$

$\partial \mathrm{F}^{\mathrm{PBE}}_{\mathrm{X}}/\partial\mu$ and $\partial \mathrm{H}/\partial\beta$ terms are derived in Appendix A. The $\partial w_a/\epsilon_{\alpha\beta}$ derivative can be written as

$$\frac{\partial w_{a'}}{\partial \epsilon_{\alpha\beta}} = \frac{\partial}{\partial \epsilon_{\alpha\beta}}\frac{\mathrm{P}_a}{\sum_{a'}\mathrm{P}_{a'}} = \frac{\frac{\partial \mathrm{P}_a}{\partial \epsilon_{\alpha\beta}}\sum_{a'}\mathrm{P}_{a'} - \mathrm{P}_a\sum_{a'}\frac{\partial \mathrm{P}_{a'}}{\partial \epsilon_{\alpha\beta}}}{\left[\sum_{a'}\mathrm{P}_{a'}\right]^2}. \tag{34}$$

To get the $\partial \mathrm{P}_a/\epsilon_{\alpha\beta}$ derivative, we use Eq. (15) of Ref. 35

$$\begin{aligned}
\frac{\partial \mathrm{P}_a}{\partial \epsilon_{\alpha\beta}} &= \frac{\partial f(|\mathbf{r} - \mathbf{R}^a|)}{\partial \epsilon_{\alpha\beta}} = \frac{\partial f(|\mathbf{r} - \mathbf{R}^a|)}{\partial r_\alpha}(r_\beta - \mathrm{R}^a_\beta) && (35) \\
&= f'(|\mathbf{r} - \mathbf{R}^a|)\frac{r_\alpha - \mathrm{R}^a_\alpha}{|\mathbf{r} - \mathbf{R}^a|}(r_\beta - \mathrm{R}^a_\beta) = \frac{\partial \mathrm{P}_a}{\partial r_\alpha}(r_\beta - \mathrm{R}^a_\beta). && (36)
\end{aligned}$$

Eqs. (24)–(36) can be used to implement the needed stress tensor corrections in GPAW, or any other "stress tensor compatible" DFT code for that matter, but it has been shown that terms like those of Eqs. (28) and (29), i.e., the ones that are a consequence of the fact that the space has been partitioned, seem to be so small that they fall below the general numerical accuracy of DFT codes.[35]

III. TEST CALCULATIONS

The correctness of the analytical QNA forces and stress tensor can be straightforwardly checked by comparing them against numerically calculated finite-difference forces and stress tensor. For example, the numerical force of atom a in the x-direction can be computed by displacing the atom by $\pm d$ along the x-direction and then calculating the finite difference $[\mathrm{E}(+d) - \mathrm{E}(-d)]/2d$. As another example, the numerical σ^{xx} component of the stress tensor is similarly computed by stretching the unit cell vector a_1 by $\pm d$ and then taking $[\mathrm{E}(+d) - \mathrm{E}(-d)]/2d\mathrm{V}$, where V is the unit cell volume. Figure 1 shows the differences between the analytical and numerical forces and σ^{xx} stress tensor component for $L1_2$ Cu_3Au. In Fig. 1, d gives the displacement of the Au atom from its (0, 0, 0) ideal lattice position along the x-axis. For the σ^{xx} stress tensor component, d indicates by how much the optimized lattice vector a_1 has been increased/decreased along the x-axis. We see that the differences between the analytical and numerical QNA forces and stress tensor are very similar to those of PBE calculated with an unadulterated version of

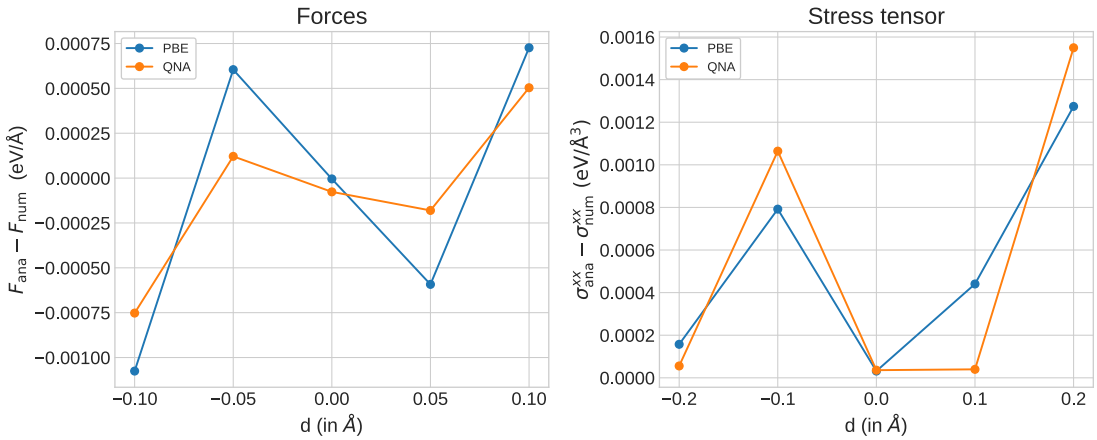

FIG. 1. The difference between the analytically and numerically calculated forces and stress tensor for $L1_2$ Cu_3Au. For forces, d means that the Au atom at (0,0,0) lattice coordinate has been shifted by d along the x-axis. For the xx component of the stress tensor, d means that the unit cell vector a_1 has been increased by d.

the GPAW code. This confirms that the equations derived in Sec. II for the analytical QNA forces and stress tensor work as expected.

As a first practical test of our implementation, we calculate the formation energies of ordered Cu–Au binary alloys. The Cu–Au system is a famous prototype in alloy theory, and it has been shown that GGA-level functionals struggle to predict the formation energies of Cu–Au binary alloys with acceptable accuracy.[17,36] Table I shows the formation energies of Cu–Au binary alloys calculated with PBE and QNA using the present GPAW implementation. We see that the GPAW results for QNA are in good agreement with the previously published EMTO results. The present GPAW implementation differs from the EMTO implementation in the way that in EMTO the space is by construction divided into Voronoi-cells that surround the muffin-tin spheres and therefore does not need the fuzzy cells formalism. Nevertheless, the results between the two codes agree, which indicates that the QNA results are not sensitive to the underlying implementation and that the stress tensor can be successfully used with QNA to optimize the unit cell geometry.

TABLE I. Formation energies of Cu–Au binary alloys. The VASP, EMTO, and experimental results are from the literature, and the GPAW results are calculated using the implementation of this paper.

	Cu_3Au ($L1_2$)	CuAu ($L1_0$)	$CuAu_2$ (β_2)	$CuAu_3$ ($L1_2$)
PBE (VASP)[36]	−44	−56	−44	−25
PBE (EMTO)[17]	−45	−57	...	−24
PBE (GPAW)	−40	−52	−41	−21
QNA (EMTO)[17]	−70	−87	...	−41
QNA (GPAW)	−71	−85	−61	−42
Expt.[36]	−74	−93	...	−39

Next, in order to test the implementation of QNA forces, we calculate mixing energies of random $Cu_{0.75}Au_{0.25}$, $Cu_{0.5}Au_{0.5}$, and $Cu_{0.25}Au_{0.75}$ alloys using 32-atom special quasirandom structures (SQSs)[38,39] generated with the Alloy Theoretic Automated Toolkit (ATAT) package.[40–42] Previous studies have found that local lattice relaxations (LLRs) are very important in Cu–Au alloys due to the large atomic size mismatch between Cu and Au atoms.[32] For random Cu–Au alloys, it is therefore important to be able to relax the atomic coordinates using forces. Figure 2 shows mixing energies of $Cu_{1-x}Au_x$ alloys as a function of x. It can be seen that the mixing energies without LLRs (labelled QNA in the figure) are positive and therefore qualitatively wrong. Mixing energies with LLRs (QNA + LLR) are much improved, and by adding a short-range order estimate at the experimental temperature from Ref. 32, we arrive at values (QNA + LLR + SRO) that are very close to the experimental values of Ref. 37.

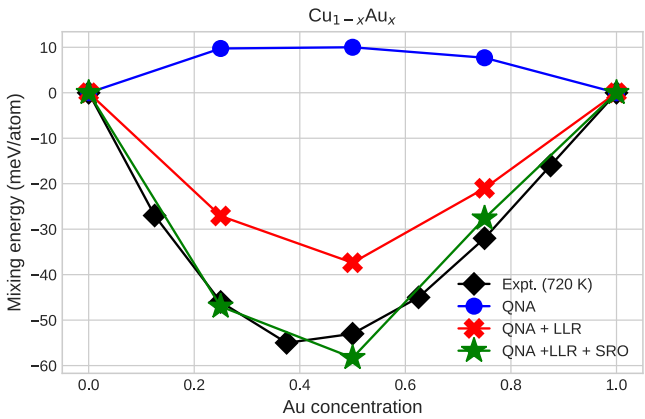

FIG. 2. Mixing energies of random $Cu_{1-x}Au_x$ alloys without LLRs (QNA), with LLRs (QNA + LLR), and with LLRs and a short-range order correction (QNA + LLR + SRO). The experimental values are from Ref. 37.

TABLE II. Formation energies ΔE (in meV/atom) and magnetic moments M_{Fe}/M_{Fe} (in μ_B) of ferromagnetic and paramagnetic Fe_3Pt alloys.

Fe_3Pt	Magnetic	XC	ΔE	M_{Fe}	M_{Pt}
	FM	LDA	−22	1.66	0.10
		PBE	−80	2.77	0.34
		PBEsol	−50	2.62	0.30
		QNA	−110	2.67	0.32
	PARA	LDA	−21	0.0	0.0
		PBE	24	2.38/−2.09	0.09
		PBEsol	16	2.20/−1.58	0.09
		QNA	−27	2.26/−1.82	0.09
Expt.[43]	FM			2.67	0.27
	FM		−34		
	FM		−96		

The good agreement of the "QNA + LLR + SRO" with experiments confirms that the QNA forces and the stress tensor are calculated correctly and with good accuracy.

As a third example, we follow Ref. 43 and calculate the formation energies and magnetic moments of ferromagnetic and paramagnetic Fe_3Pt in $L1_2$ structure. In the ferromagnetic state, all moments point in the same direction, and in order to simulate the paramagnetic state, one of the Fe moments is inverted with respect to the other two Fe atoms in the unit cell. We used Fe and Pt PAW-setups similar to Ref. 43, where 3*d*74*s*1 and 5*d*96*s*1 are treated as valence electrons for Fe and Pt, respectively. We also tried both the "MixerSum" and "MixerDif" density mixing methods that GPAW offers because in some cases there is a difference between the magnetic states (and the ground-state energies) to which the two mixers converge. Table II shows our results calculated with four different XC functionals, which are LDA, PBE, PBEsol, and QNA. Calculations were run using two different density mixers mentioned above, and in each case, the results in Table II correspond to whichever mixer that yielded the lower ground-state energy. Unlike Ref. 43, all four XC functionals predict the ferromagnetic state (FM) to be more stable than the paramagnetic state (PARA), although for LDA the difference between FM and PARA formation energies is very small. The magnitudes of LDA formation energy and magnetic moments are underestimated compared to the available experimental values. PBE and PBEsol predict FM formation energies that are between the two experimental values, but PBEsol magnetic moments are slightly closer to experiments than those of PBE. QNA predicts a formation energy that slightly overestimates the available experimental data, but like PBEsol the QNA magnetic moments are in very good agreement with experiments. Overall, we can say that our QNA implementation is viable also for magnetic alloys.

IV. CONCLUSIONS

We have implemented the Becke fuzzy cells type space partitioning scheme in GPAW for the purposes of the flexible GGA-level QNA exchange-correlation functional and tested its functionality for a few test systems. In general, space partitioning allows one to define atomic site specific quantities or to divide the system at hand into physically different regions, such as a bulk region and surface regions. Since the bulk and surface regions could now be calculated with separate exchange-correlation functionals that are specifically designed to capture the important physics of those regions, space partitioning is one possible route to improved DFT accuracy.

ACKNOWLEDGMENTS

M.K. acknowledges the Academy of Finland (Grant No. 295602). The computer resources of the Finnish IT Center for Science (CSC) and the Finnish Grid and Cloud Infrastructure (FGCI) project (Finland), and the Swedish National Infrastructure for Computing (SNIC) at the High Performance Computing Center North (HPC2N) are acknowledged.

APPENDIX A: EQUATIONS

By taking the partial derivative with respect to the nuclear position of Eq. (12), the QNA XC force contribution within the PAW formalism is of the form

$$\begin{aligned}
\mathbf{F}^a_{\mathrm{XC}} = -\frac{\partial \mathrm{E}_{\mathrm{XC}}[\tilde{n}]}{\partial \mathbf{R}^a} = -\int \mathrm{d}\mathbf{r}\Bigg(&\frac{\delta \mathrm{E}_{\mathrm{XC}}[\tilde{n}(\mathbf{r}),\tilde{\mu}(\mathbf{r}),\tilde{\beta}(\mathbf{r})]}{\delta \tilde{n}(\mathbf{r})}\frac{\partial \tilde{n}(\mathbf{r})}{\partial \mathbf{R}^a} + \frac{\delta \mathrm{E}_{\mathrm{XC}}[\tilde{n}(\mathbf{r}),\tilde{\mu}(\mathbf{r}),\tilde{\beta}(\mathbf{r})]}{\delta \tilde{\mu}(\mathbf{r})}\frac{\partial \tilde{\mu}(\mathbf{r})}{\partial \mathbf{R}^a} + \frac{\delta \mathrm{E}_{\mathrm{XC}}[\tilde{n}(\mathbf{r}),\tilde{\mu}(\mathbf{r}),\tilde{\beta}(\mathbf{r})]}{\delta \tilde{\beta}(\mathbf{r})}\frac{\partial \tilde{\beta}(\mathbf{r})}{\partial \mathbf{R}^a}\Bigg) \\
&- \sum_a \sum_{ii'} \int \mathrm{d}\mathbf{r}\Bigg(\frac{\delta \mathrm{E}^a_{\mathrm{XC}}[n^a(\mathbf{r}),\mu^a(\mathbf{r}),\beta^a(\mathbf{r})]}{\delta n^a(\mathbf{r})}\frac{\partial n^a(\mathbf{r})}{\partial \mathrm{D}^a_{ii'}} + \frac{\delta \mathrm{E}^a_{\mathrm{XC}}[\tilde{n}^a(\mathbf{r}),\mu^a(\mathbf{r}),\beta^a(\mathbf{r})]}{\delta \tilde{n}^a(\mathbf{r})}\frac{\partial n^a(\mathbf{r})}{\partial \mathrm{D}^a_{ii'}}\Bigg)\frac{\partial \mathrm{D}^a_{ii'}}{\partial \mathbf{R}^a} \\
&- \sum_a \sum_{ii'} \int \mathrm{d}\mathbf{r}\Bigg(\frac{\delta \mathrm{E}^a_{\mathrm{XC}}[n^a(\mathbf{r}),\mu^a(\mathbf{r}),\beta^a(\mathbf{r})]}{\delta \mu^a(\mathbf{r})}\frac{\partial \mu^a(\mathbf{r})}{\partial \mathrm{D}^a_{ii'}} + \frac{\delta \mathrm{E}^a_{\mathrm{XC}}[\tilde{n}^a(\mathbf{r}),\mu^a(\mathbf{r}),\beta^a(\mathbf{r})]}{d\tilde{\mu}^a(\mathbf{r})}\frac{\partial \tilde{\mu}^a(\mathbf{r})}{\partial \mathrm{D}^a_{ii'}}\Bigg)\frac{\partial \mathrm{D}^a_{ii'}}{\partial \mathbf{R}^a} \\
&+ \sum_a \sum_{ii'} \int \mathrm{d}\mathbf{r}\Bigg(\frac{\delta \mathrm{E}^a_{\mathrm{XC}}[n^a(\mathbf{r}),\mu^a(\mathbf{r}),\beta^a(\mathbf{r})]}{d\beta^a(\mathbf{r})}\frac{\partial \beta^a(\mathbf{r})}{\partial \mathrm{D}^a_{ii'}} + \frac{\delta \mathrm{E}^a_{\mathrm{XC}}[\tilde{n}^a(\mathbf{r}),\mu^a(\mathbf{r}),\beta^a(\mathbf{r})]}{d\tilde{\beta}^a(\mathbf{r})}\frac{\partial \tilde{\beta}^a(\mathbf{r})}{\partial \mathrm{D}^a_{ii'}}\Bigg)\frac{\partial \mathrm{D}^a_{ii'}}{\partial \mathbf{R}^a}.
\end{aligned} \tag{A1}$$

In Eqs. (18) and (19), the partial derivatives

$$\frac{\partial\left\{\tilde{n}(\mathbf{r})\varepsilon_{XC}^{PBE}[\tilde{n}(\mathbf{r}),|\nabla\tilde{n}(\mathbf{r})|^2,\tilde{\mu}(\mathbf{r}),\tilde{\beta}(\mathbf{r})]\right\}}{\partial\tilde{\mu}(\mathbf{r})}, \quad \frac{\partial\left\{\tilde{n}(\mathbf{r})\varepsilon_{XC}^{PBE}[\tilde{n}(\mathbf{r}),|\nabla\tilde{n}(\mathbf{r})|^2,\tilde{\mu}(\mathbf{r}),\tilde{\beta}(\mathbf{r})]\right\}}{\partial\tilde{\beta}(\mathbf{r})},$$

when written out, become

$$\frac{\partial\left\{\tilde{n}(\mathbf{r})\varepsilon_{XC}^{PBE}[\tilde{n}(\mathbf{r}),|\nabla\tilde{n}(\mathbf{r})|^2,\tilde{\mu}(\mathbf{r}),\tilde{\beta}(\mathbf{r})]\right\}}{\partial\tilde{\mu}(\mathbf{r})} = \frac{\partial\left[\tilde{n}(\mathbf{r})\varepsilon_X^{LDA}\left(F_X^{PBE}[\tilde{n}(\mathbf{r}),|\nabla\tilde{n}(\mathbf{r})|^2,\tilde{\mu}(\mathbf{r})]+\left\{\frac{\varepsilon_C^{LDA}}{\varepsilon_X^{LDA}}+\frac{H[\tilde{n}(\mathbf{r}),|\nabla\tilde{n}(\mathbf{r})|^2,\tilde{\beta}(\mathbf{r})]}{\varepsilon_X^{LDA}}\right\}\right)\right]}{\partial\tilde{\mu}(\mathbf{r})}$$
$$= \tilde{n}(\mathbf{r})\varepsilon_X^{LDA}\frac{\partial F_X^{PBE}}{\partial\tilde{\mu}} = \tilde{n}(\mathbf{r})\varepsilon_X^{LDA}\left[\frac{s^2}{(1+\mu s^2/\kappa)^2}\right], \tag{A2}$$

$$\frac{\partial\left\{\tilde{n}(\mathbf{r})\varepsilon_{XC}^{PBE}[\tilde{n}(\mathbf{r}),|\nabla\tilde{n}(\mathbf{r})|^2,\tilde{\mu}(\mathbf{r}),\tilde{\beta}(\mathbf{r})]\right\}}{\partial\tilde{\beta}(\mathbf{r})} = \frac{\partial\left[\tilde{n}(\mathbf{r})\varepsilon_X^{LDA}\left(F_X^{PBE}[\tilde{n}(\mathbf{r}),|\nabla\tilde{n}(\mathbf{r})|^2,\tilde{\mu}(\mathbf{r})]+\left\{\frac{\varepsilon_C^{LDA}}{\varepsilon_X^{LDA}}+\frac{H[\tilde{n}(\mathbf{r}),|\nabla\tilde{n}(\mathbf{r})|^2,\tilde{\beta}(\mathbf{r})]}{\varepsilon_X^{LDA}}\right\}\right)\right]}{\partial\tilde{\beta}(\mathbf{r})}$$
$$= \tilde{n}(\mathbf{r})\frac{\partial H}{\partial\beta} = \frac{Yt^2}{X\gamma}\left[\frac{1+2At^2}{1+At^2+A^2t^4}-\frac{(1+At^2)(At^2+2A^2t^4)}{(1+At^2+A^2t^4)^2}\right], \tag{A3}$$

where we have used the notation of Ref. 6 as

$$Y = \frac{e^2}{a_0}\gamma\phi^3, \tag{A4}$$

$$H = Y\times\ln\left\{1+\frac{\beta}{\gamma}t^2\left[\frac{1+At^2}{1+At^2+A^2t^4}\right]\right\}, \tag{A5}$$

$$X = 1+\frac{\beta}{\gamma}t^2\left[\frac{1+At^2}{1+At^2+A^2t^4}\right], \tag{A6}$$

$$A = \frac{\beta}{\gamma}\left[\exp\left\{-\varepsilon_c^{LDA}/Y\right\}-1\right]^{-1}, \tag{A7}$$

$$\frac{\delta A}{\delta\beta} = \frac{A}{\beta}, \tag{A8}$$

where e is the elementary charge, a_0 is the Bohr radius, $\gamma = (1-\ln 2)/\pi^2$, and $\phi = [(1+\zeta)^{2/3}+(1-\zeta)^{2/3}]/2$, where $\zeta = (n_\uparrow - n_\downarrow)/n$ is the relative spin polarization.

APPENDIX B: COMPUTATIONAL DETAILS

The analytical force and stress tensor test used the planewave mode with an energy cutoff of 600 eV and a 10 × 10 × 10 grid of Monkhorst-Pack k-points.[44] The version 0.9.20 000 of PAW setups was used. Fermi-Dirac smearing was used with a width of 0.01 eV.

The ordered Cu–Au calculations used the planewave mode and an energy cutoff of 550 eV. The Monkhorst-Pack scheme was used to generate the k-point grids whose sizes were 20 × 20 × 20. The version 0.9.20 000 of PAW setups was used. Fermi-Dirac smearing was used with a width of 0.01 eV.

The 32-atom CuAu SQS calculations used the planewave mode and an energy cutoff of 550 eV. Forces were relaxed until the largest remaining force was smaller than 0.01 eV, which ensured that the mixing energies were converged. A 10 × 10 × 10 grid of Monkhorst-Pack k-points was used. The version 0.9.20 000 of PAW setups was used. Fermi-Dirac smearing was used with a width of 0.01 eV.

The Fe_3Pt calculations used the planewave basis and an energy cutoff of 600 eV. We used Fe and Pt PAW-setups similar to Ref. 43, where 3d74s1 and 5d96s1 are treated as valence electrons for Fe and Pt, respectively. We used 10 × 10 × 10 and 15 × 15 × 15 Monkhorst-Pack k-point grids for $L1_2$ (Fe_3Pt, bulk Pt) and B_2 (bulk Fe) structures, respectively. Fermi-Dirac smearing was used with a width of 0.1 eV. MixerSum and MixerDif density mixers used the following settings: {backend: pulay, beta: 0.02, nmaxold: 1, weight: 100}. In the MixerSum scheme, the spin channels of the density matrices are mixed separately and the spin channels of the pseudo electron density is mixed as a sum. In the MixerDif scheme, both the total density and magnetization densities are mixed separately.

REFERENCES

[1] P. Hohenberg and W. Kohn, Phys. Rev. **136**, B864 (1964).
[2] W. Kohn and L. J. Sham, Phys. Rev. **140**, A1133 (1965).
[3] S. H. Vosko, L. Wilk, and M. Nusair, Can. J. Phys. **58**, 1200 (1980).
[4] J. P. Perdew and A. Zunger, Phys. Rev. B **23**, 5048 (1981).
[5] J. P. Perdew and Y. Wang, Phys. Rev. B **45**, 13244 (1992).
[6] J. P. Perdew, K. Burke, and M. Ernzerhof, Phys. Rev. Lett. **77**, 3865 (1996).
[7] S. K. Ghosh and R. G. Parr, Phys. Rev. A **34**, 785 (1986).
[8] A. D. Becke and M. R. Roussel, Phys. Rev. A **39**, 3761 (1989).
[9] J. Tao, J. P. Perdew, V. N. Staroverov, and G. E. Scuseria, Phys. Rev. Lett. **91**, 146401 (2003); e-print arXiv:0306203 [cond-mat].
[10] A. D. Becke, J. Chem. Phys. **98**, 1372 (1993).
[11] A. D. Becke, J. Chem. Phys. **98**, 5648 (1993).
[12] F. Tran, J. Stelzl, and P. Blaha, J. Chem. Phys. **144**, 204120 (2016).
[13] Z. Wu and R. E. Cohen, Phys. Rev. B **73**, 235116 (2006).
[14] J. P. Perdew, A. Ruzsinszky, G. I. Csonka, O. A. Vydrov, G. E. Scuseria, L. A. Constantin, X. Zhou, and K. Burke, Phys. Rev. Lett. **100**, 136406 (2008).
[15] Y. Zhao and D. G. Truhlar, J. Chem. Phys. **128**, 184109 (2008).
[16] L. A. Constantin, A. Terentjevs, F. Della Sala, P. Cortona, and E. Fabiano, Phys. Rev. B **93**, 045126 (2016).

[17]L.-Y. Tian, H. Levämäki, M. Ropo, K. Kokko, Á. Nagy, and L. Vitos, Phys. Rev. Lett. **117**, 066401 (2016).
[18]A. D. Becke, J. Chem. Phys. **88**, 2547 (1988).
[19]H. Levämäki, M. P. J. Punkkinen, K. Kokko, and L. Vitos, Phys. Rev. B **86**, 201104 (2012).
[20]H. Levämäki, M. P. J. Punkkinen, K. Kokko, and L. Vitos, Phys. Rev. B **89**, 115107 (2014).
[21]J. J. Mortensen, L. B. Hansen, and K. W. Jacobsen, Phys. Rev. B **71**, 035109 (2005).
[22]J. Enkovaara, C. Rostgaard, J. J. Mortensen, J. Chen, M. Dułak, L. Ferrighi, J. Gavnholt, C. Glinsvad, V. Haikola, H. A. Hansen, H. H. Kristoffersen, M. Kuisma, A. H. Larsen, L. Lehtovaara, M. Ljungberg, O. Lopez-Acevedo, P. G. Moses, J. Ojanen, T. Olsen, V. Petzold, N. A. Romero, J. Stausholm-Møller, M. Strange, G. A. Tritsaris, M. Vanin, M. Walter, B. Hammer, H. Häkkinen, G. K. H. Madsen, R. M. Nieminen, J. K. Nørskov, M. Puska, T. T. Rantala, J. Schiøtz, K. S. Thygesen, and K. W. Jacobsen, J. Phys.: Condens. Matter **22**, 253202 (2010).
[23]O. K. Andersen, O. Jepsen, and G. Krier, in *Lectures on Methods of Electronic Structure Calculations*, January 1994, edited by V. Kumar, O. K. Andersen, and A. Mookerjee (World Scientific, Singapore, 1995), pp. 63–124.
[24]L. Vitos, I. A. Abrikosov, and B. Johansson, Phys. Rev. Lett. **87**, 156401 (2001).
[25]L. Vitos, Phys. Rev. B **64**, 014107 (2001).
[26]L. Vitos, *Computational Quantum Mechanics for Materials Engineers*, Engineering Materials and Processes (Springer-Verlag, 2007).
[27]P. E. Blöchl, Phys. Rev. B **50**, 17953 (1994).
[28]G. Kresse and D. Joubert, Phys. Rev. B **59**, 1758 (1999).
[29]S. Bahn and K. Jacobsen, Comput. Sci. Eng. **4**, 56 (2002).
[30]A. Hjorth Larsen, J. Jørgen Mortensen, J. Blomqvist, I. E. Castelli, R. Christensen, M. Dułak, J. Friis, M. N. Groves, B. Hammer, C. Hargus, E. D. Hermes, P. C. Jennings, P. Bjerre Jensen, J. Kermode, J. R. Kitchin, E. Leonhard Kolsbjerg, J. Kubal, K. Kaasbjerg, S. Lysgaard, J. Bergmann Maronsson, T. Maxson, T. Olsen, L. Pastewka, A. Peterson, C. Rostgaard, J. Schiøtz, O. Schütt, M. Strange, K. S. Thygesen, T. Vegge, L. Vilhelmsen, M. Walter, Z. Zeng, and K. W. Jacobsen, J. Phys.: Condens. Matter **29**, 273002 (2017).
[31]M. Franchini, P. H. T. Philipsen, and L. Visscher, J. Comput. Chem. **34**, 1819 (2013).
[32]L.-Y. Tian, L.-H. Ye, Q.-M. Hu, S. Lu, and J. Zhao, Comput. Mater. Sci. **128**, 302 (2017).
[33]P. Salvador and E. Ramos-Cordoba, J. Chem. Phys. **139**, 071103 (2013).
[34]A. H. Larsen, M. Vanin, J. J. Mortensen, K. S. Thygesen, and K. W. Jacobsen, Phys. Rev. B **80**, 195112 (2009).
[35]F. Knuth, C. Carbogno, V. Atalla, V. Blum, and M. Scheffler, Comput. Phys. Commun. **190**, 33 (2015).
[36]Y. Zhang, G. Kresse, and C. Wolverton, Phys. Rev. Lett. **112**, 075502 (2014).
[37]R. Orr, Acta Metall. **8**, 489 (1960).
[38]A. Zunger, S.-H. Wei, L. G. Ferreira, and J. E. Bernard, Phys. Rev. Lett. **65**, 353 (1990).
[39]S. H. Wei, L. G. Ferreira, J. E. Bernard, and A. Zunger, Phys. Rev. B **42**, 9622 (1990).
[40]A. van de Walle, M. D. Asta, and G. Ceder, Calphad **26**, 539 (2002).
[41]A. van de Walle, Calphad **33**, 266 (2009).
[42]A. van de Walle, P. Tiwary, M. M. de Jong, D. L. Olmsted, M. D. Asta, A. Dick, D. Shin, Y. Wang, L.-Q. Chen, and Z.-K. Liu, Calphad **42**, 13 (2013).
[43]A. H. Romero and M. J. Verstraete, Eur. Phys. J. B **91**, 193 (2018).
[44]H. J. Monkhorst and J. D. Pack, Phys. Rev. B **13**, 5188 (1976).